

Manganese-Doped Zirconia Nanocrystals

Guylhaine Clavel,^[a] Marc-Georg Willinger,^[a,b] David Zitoun,^{*[c]} and Nicola Pinna^{*[a]}

Keywords: Zirconium / Manganese / Doping / Magnetic properties / Nanoparticles

In recent theoretical work, it was predicted that transition-metal-doped zirconia (ZrO_2) can be ferromagnetic at room temperature with a dependence on the metal dopant and its oxidation state and concentration.^[1] For experimental verification of these predictions, manganese-doped ZrO_2 nanoparticles were synthesized. The synthesis was achieved by the benzyl alcohol route, which led to high-quality nanocrystals with uniform size and shape. The obtained particles present a homogeneous distribution of the magnetic ion. The crystallographic phase was studied by XRD, electron diffraction,

and high-resolution TEM. The doping efficiency was determined at the macroscopic level by chemical analysis and at the nanoscale level by electron energy loss spectrometry. The local structure of the manganese ions in the ZrO_2 matrix was characterized by electron paramagnetic resonance. Finally, the magnetic properties of the obtained nanocrystals were investigated by susceptibility measurements.

(© Wiley-VCH Verlag GmbH & Co. KGaA, 69451 Weinheim, Germany, 2008)

Introduction

Materials based on zirconia (ZrO_2) display good thermal stability and interesting acid–base and redox properties, and they also have the advantage of a very low cost. As a consequence, zirconia is a leading material used in industry with applications in catalysis, ceramics, and in solid-oxide fuel cells.^[2–4] ZrO_2 can crystallize in a monoclinic, cubic, or tetragonal phase.^[5] One of the major challenges is therefore to control and tune the crystallographic phase. In view of its applications, the cubic phase is the most suitable. Although this phase is metastable, it can be stabilized by the addition of another cation in the structure, mainly yttrium, but also magnesium, calcium, gadolinium, and cadmium; moreover, the concentration of the cation plays an important role.^[6–11] In the literature, many studies have centered on the local environment of the stabilizing ion by means of electron paramagnetic resonance (EPR).^[12–14] Interestingly, doped ZrO_2 was rarely considered as a potential material for its electronic properties. Furthermore, the study of the magnetic properties of zirconia doped with magnetic ions (e.g. Mn, Co, Fe, etc.) was almost completely neglected. Indeed, one study only reported the magnetic properties when zirconia was doped with manganese.^[15]

Recently, the field of transition-metal-doped oxides was dominated by the quest for high-temperature ferromagnetic

semiconductors, so called diluted magnetic semiconductors (DMS). Most of the theoretical and experimental studies focused on zinc oxide or gallium nitride. These materials gave rise to further investigation on very large bandgap semiconductors, as they were predicted ferromagnetic above room temperature when doped with magnetic ions. Materials possessing the required characteristics are scarce. As recently predicted by Ostanin et al.,^[1] doped ZrO_2 should be considered as one of the few suitable materials.

In this manuscript, we present a benzyl-alcohol-based synthesis^[16–19] of highly crystalline and monodisperse ZrO_2 nanoparticles that are doped with up to 5% of Mn. This synthetic approach in general leads to nanosized particles that are well suited for decent characterization by various techniques including high-resolution TEM, EELS, and EPR. The synthesized particles are presented here as an ideal system for studying the effect of Mn doping on the magnetic properties of the material. This is of special interest in view of recent theoretical investigations aimed at the prediction of new DMS materials.

Results and Discussion

The condensation reaction leading to the formation of zirconia is an ether elimination occurring between zirconium isopropoxide and benzyl alcohol,^[20] similarly to what was found previously for the formation of HfO_2 .^[21] In the case of zirconia, the particles exhibit a uniformly spherical morphology with a narrow size distribution of 3–4 nm and particles can be produced in multigram-scale quantities.^[17,20,22] Doping of ZrO_2 was performed by the addition of a quantity of manganese(II) acetate or, alternatively, of manganese(III) acetylacetonate to the reaction mixture. In

[a] Department of Chemistry, CICECO, University of Aveiro, 3810-193 Aveiro, Portugal
E-mail: pinna@ua.pt

[b] Fritz Haber Institut of the Max Planck Society, Department of Inorganic Chemistry, Faradayweg 4–6, 14195 Berlin, Germany

[c] AIME, Institut Charles Gerhardt, Université Montpellier II, Place Eugène Bataillon, 34095 Montpellier, France
E-mail: zitoun@univ-montp2.fr

both cases, pale-brown powders were obtained. The doping concentration after the synthesis was monitored by ICP-AES measurements and was found to range from 1 to 5% (Table 1). The effectiveness of the doping is elevated, and it ranges from around 80% for $\text{Mn}(\text{ac})_2$ to 90% in the case of $\text{Mn}(\text{acac})_3$.

Table 1. Manganese-doped samples studied in this work. The table shows the inorganic precursors used, the atomic concentration of Mn in zirconia [$\text{Zr}_{(1-x)}\text{Mn}_x\text{O}_2$], and the oxidation state of the manganese as estimated from EPR measurements. Magnetic moments at saturation (Msat) were determined from a Langevin fit of the magnetization curves.

Sample	Mn precursor	$x = \% \text{Mn}$ (ICP-AES)	$\% \text{Mn}^{2+}$ (EPR)	$\% \text{Mn}^{3+}$ (EPR)	Msat [μ_B/Mn]
I	$\text{Mn}(\text{acac})_3$	1.20	69 ± 2	31 ± 2	4.33
II	$\text{Mn}(\text{ac})_2$	1.39	61 ± 2	39 ± 2	4.27
III	$\text{Mn}(\text{ac})_2$	4.38	9 ± 2	91 ± 2	3.55
IV	$\text{Mn}(\text{acac})_3$	4.85	8 ± 2	92 ± 2	3.40

X-ray diffraction patterns of the as-synthesized pure and doped zirconia particles are displayed in Figure 1. They show broad diffraction peaks due to the nanometric size of the zirconia crystals. No additional reflections of crystalline impurities are observed even for the most doped sample. An average particle size of approximately 3–4 nm, as deduced by the Scherrer formula, is obtained for both pure and doped zirconia particles. As the diffraction peaks are broad, XRD experiments are not suitable to assign univocally the crystalline structure of the nanoparticles. Indeed, lattice parameters of the cubic (JCPDS [27–997]) and tetragonal phase (JCPDS [17–923]) of zirconia are similar, and XRD patterns only differ in a few and very close reflections (cf. vertical bar Figure 1). However, on the basis of Rietveld refinement, it was shown that the synthetic procedure leads to the cubic phase.^[20] Contrarily to the bulk phase at the nanoscale, the cubic or tetragonal structure does not need to be stabilized by the addition of another ion.^[23–28]

Observation of the synthesized products by transmission electron microscopy (TEM) reveals particles of highly homogeneous size and shape (Figure 2). The spherical particles have an average diameter of 3 to 4 nm and appear at random orientation on the supporting carbon film of the TEM grid. At high magnification, the crystalline particles show lattice fringes. The distances and angles between the corresponding lattice planes were abstracted from the Fourier-transformed high-resolution images. They are in good agreement with the cubic ZrO_2 phase for both the Mn-doped and the undoped sample.

Figure 2 shows overview and high-resolution TEM micrographs as well as the power spectra from single particles in the [110] direction. The particles are monocrystalline in nature and do not present any core defaults. Because of the small size of the particles, the precision in the measurement of the lattice spacing from high-resolution images is limited. Therefore, slight changes in the lattice spacing that might eventually be induced by the dopant cannot be detected. This was expected, as no shift in the lattice spac-

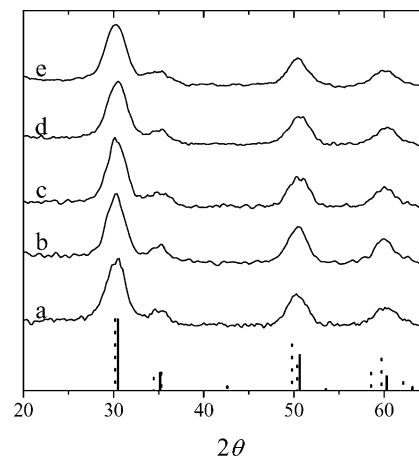


Figure 1. XRD patterns of (a) undoped zirconia; (b) zirconia doped with 1.39% of $\text{Mn}(\text{ac})_2$; (c) zirconia doped with 1.20% of $\text{Mn}(\text{acac})_3$; (d) zirconia doped with 4.38% of $\text{Mn}(\text{ac})_2$; (e) zirconia doped with 4.85% of $\text{Mn}(\text{acac})_3$. Theoretical reflection of cubic phase (vertical full line) and tetragonal phase (vertical dotted line) are specified.

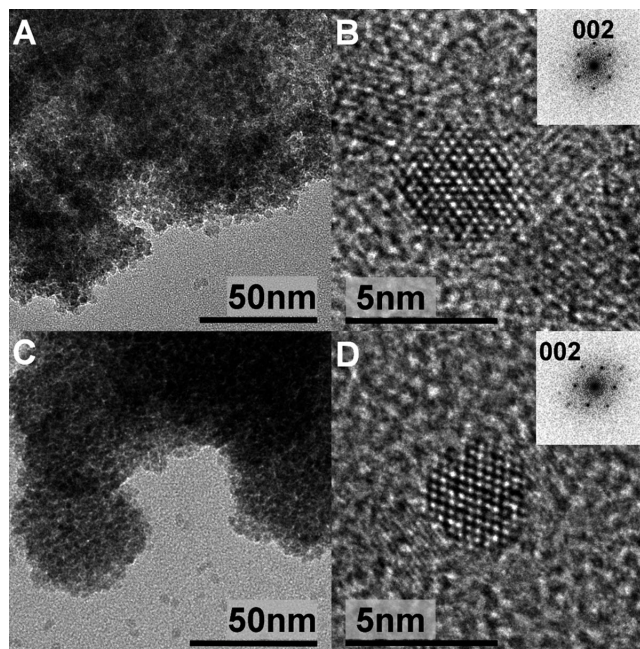


Figure 2. (A) TEM overview image showing an agglomeration of 4.38% Mn-ZrO_2 doped particles synthesized from $\text{Mn}(\text{ac})_2$; (B) corresponding HRTEM image of a particle in the [110] orientation with the respective power spectrum (inset); (C) TEM image of pure zirconia sample; (D) corresponding HRTEM picture showing a single particle in the [110] orientation and its power spectrum.

ing was detected by XRD either. In fact, the amount of Mn in the ZrO_2 is too low in order to significantly modify the lattice parameters.

In order to investigate the distribution of manganese, electron energy loss spectrometry (EELS) was applied. EELS is a very sensitive technique and perfectly suitable for analyzing the chemical composition of materials at the nanometer scale. EELS spectra recorded in the energy range covering the oxygen K edge at around 530 eV and

the manganese $L_{2,3}$ edges at 638 (L_3) and 649 eV (L_2), respectively, are presented in Figure 3. The spectra were recorded from sample III (high doping) at different regions containing varying numbers of particles in order to draw conclusions about the homogeneity of the Mn distribution (Figure 3, A–C). In all presented spectra, the background was removed and zero-loss deconvolution for the removal of the intensity due to plural inelastic scattering was performed. A clear manganese $L_{2,3}$ edge is visible in all the obtained spectra; although, according to the ICP-AE measurements, only 4.38% of the zirconium atoms were replaced by manganese. In general, the relative intensities of the Mn L_2 and L_3 edges and their integrated intensities are a sensible measure for the manganese oxidation state and its quantity.^[29] In the present case, the low amount of Mn in combination with the small particle size result in a bad signal-to-noise ratio, which prevents precise determination of these quantities.

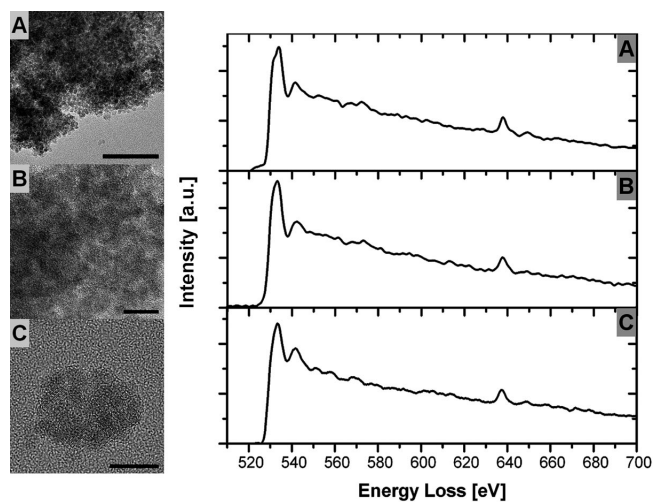


Figure 3. EELS spectra recorded from different agglomerations of 4.38% Mn-doped particles (A), (B), and (C). The TEM images show the amount of particles that have contributed to each spectrum. Scale bars correspond to 50, 10, and 10 nm for A, B, and C, respectively.

Besides the low signal-to-noise ratios, removal of the background and deconvolution are also responsible for most of the observed differences in the spectra. This is due to the fact that both background subtraction and zero-loss deconvolution were done for spectra that were recorded under non ideal conditions, that is, from regions containing inhomogeneous distributions of particles. Nevertheless, on the basis of the presence of the manganese $L_{2,3}$ edges in all spectra and independent of the amount of particles from which the signal was recorded, a homogeneous distribution of manganese in the particles is concluded.

The local environment and oxidation state of the Mn ions was probed with electron paramagnetic resonance (EPR) on powder samples. EPR is a sensitive probe and was previously used for the investigation of transition-metal impurities on surfaces or in dilute solid solutions.^[15,30–32] In the present case, the nanocrystals can be regarded as a collection of diluted spins that are randomly distributed in

the oxide matrix. Therefore, EPR measurements provide information about the oxidation state, the local symmetry, and the spin–spin interactions. Figure 4 shows a characteristic EPR spectrum recorded at room temperature. In a set of experiments, the temperature was varied from 300 down to 6 K. No change in the spectrum, except for an increase in the signal amplitude, was observed. In zirconia, the manganese ions can exist or coexist in three different oxidation states (II, III, and IV). Mn^{2+} and Mn^{4+} show similar, but discernible resonances, whereas the Mn^{3+} ion is EPR “silent”.^[33] The lack of signals for Mn^{3+} is due to the large value of the zero-field splitting that occurs for most of the local environments (i.e., crystal fields), which shifts the EPR signal out of the energy regime of conventional X-band spectrometers.^[34]

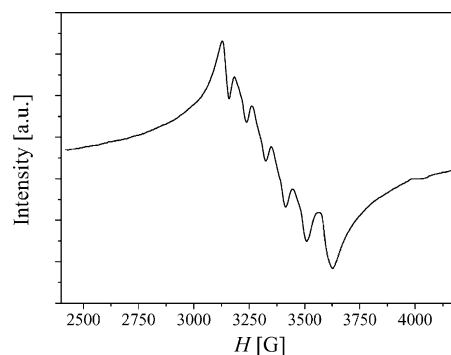


Figure 4. EPR spectrum recorded at room temperature for sample I [1.20% Mn from $Mn(acac)_3$ precursor].

All recorded spectra display two contributions centered at $g = 2.020$ (Figure 4): (1) a broad resonance resulting from magnetic interactions of the Mn ions and (2) a sextuplet from isolated spins. The observed hyperfine splitting [$A = 86(1)$ Gauss] corresponds to the usual values for Mn^{2+} . The g factor of Mn^{2+} ($3d^5$, $g_0 = 2.00$) and Mn^{4+} ($3d^3$, $g_0 = 1.98$) are very close to each other. However, the A value is usually found to be lower in the case of Mn^{4+} [$A = 78(1)$ Gauss]. By taking into account the g factor and the A value, the EPR signal is then assumed to be mainly dominated by the contribution of Mn^{2+} . This analysis is in agreement with a previous study where EPR analysis revealed isolated Mn^{2+} in zirconia.^[33]

A manganese salt [manganese(II)acetate, hydrated] diluted in a matrix and Mn-doped ZnO were used as references to perform quantitative EPR analysis.^[35] Mn-doped zinc oxide is a suitable reference, as it is a DMS itself that contains Mn in a 2+ oxidation state.^[35] The nominal content of Mn^{2+} in ZrO_2 was evaluated from the double integral of the respective EPR signals after a baseline correction. In all cases, the amount of Mn^{2+} was found to be lower than the manganese total concentration derived from ICP-AES measurements. The amount of Mn^{3+} was therefore deduced by simple subtraction (Table 1).

First order analysis of the data therefore revealed the presence of manganese in two oxidation states (II and III). An interesting point is the relation between the manganese concentration and its oxidation state. For diluted samples I

and II, Mn^{II} is the predominant species, and its concentration is independent of the oxidation state of the precursor used (Table 1). From this, it follows that for the highly diluted samples each Mn atom in the zirconia matrix should be associated to one oxygen vacancy.

An increase in the Mn concentration from 1 to 5 atomic% leads to a decrease in the paramagnetic signal. This can be attributed to the oxidation of some Mn^{II} towards the EPR-silent Mn^{III} . The estimated Mn^{III} content is larger than that of Mn^{II} for the most-concentrated samples (Table 1). To confirm this hypothesis, a technique suitable for the characterization of the Mn oxidation state, such as XPS, should be used.

Magnetic Properties

After providing evidence for the homogeneity of doping and the absence of any secondary phase, the magnetic properties of the DMS can now be safely discussed. The magnetic measurements were performed at low and high field as a function of manganese concentration and oxidation state of the inorganic precursor used. The susceptibility was investigated by using a zero-field-cooled/field-cooled routine at low field ($\mu_0 H = 5.0$ mT). Figure 5 shows the results

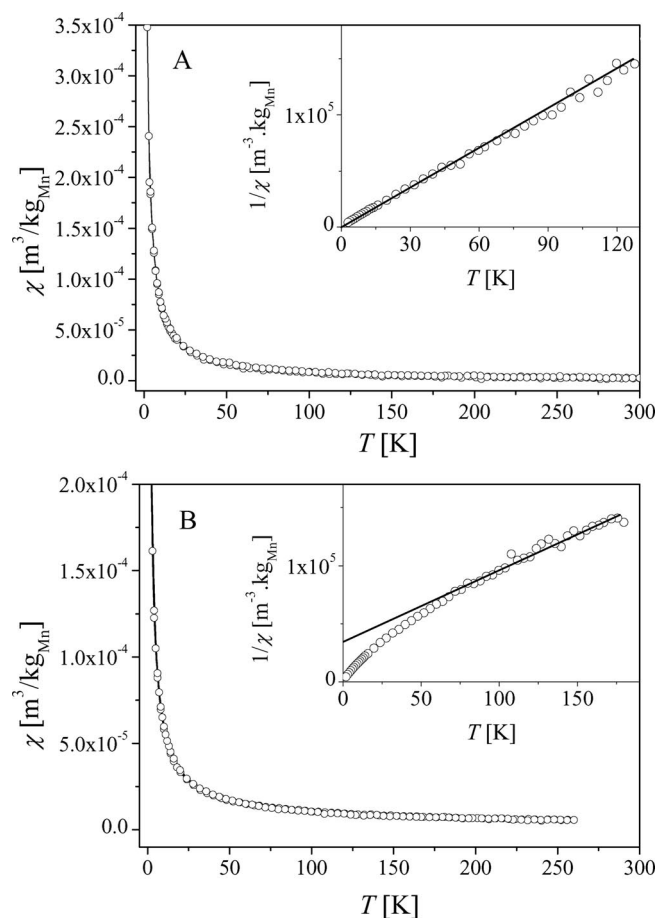


Figure 5. ZFC/FC curves measured in a field of 50 Oe for (A) a diluted sample from $\text{Mn}(\text{acac})_3$ with 1.20% Mn and (B) a concentrated sample from $\text{Mn}(\text{ac})_2$ with 4.38% Mn. In both cases, the insets show the inverse of the susceptibility and a linear fit.

for two different Mn concentrations. The susceptibility and the inverse of the susceptibility are both plotted as a function of temperature. All samples display paramagnetic behavior. For the most-diluted sample (Sample I, 1.20% Mn), the inverse of susceptibility follows a Curie law with a parameter $C = 8.85 \times 10^{-4} \text{ emu K g}_{\text{Mn}}^{-1}$ and a Curie–Weiss temperature of $\theta = (-0.4 \pm 0.2)$ K. For the sample with the highest Mn concentration (Sample III, 4.38% Mn), the same parameters reach the values of $C = 1.16 \times 10^{-3} \text{ emu K g}_{\text{Mn}}^{-1}$ and $\theta = (-50 \pm 2)$ K. From the Curie constants, the spontaneous moment per Mn atom can be determined $M_S = 4.4(1)$ and $3.8(1) \mu_B/\text{Mn}$ for Sample I and III, respectively.

As the samples showed a pure paramagnetic behavior at room temperature, additional high-field measurements, $M(H)$, were performed at low temperature ($T = 2$ K). The results are plotted in Bohr magnetons per manganese atom (μ_B/Mn) for the samples synthesized from $\text{Mn}(\text{ac})_2$ and $\text{Mn}(\text{acac})_3$ in Figure 6a and b, respectively. All doped samples display a hysteresis. The coercive field reaches 1.7 mT for the 4.38 and 4.85% Mn-doped samples and 0.4 mT for the most diluted samples. The observed hysteresis results

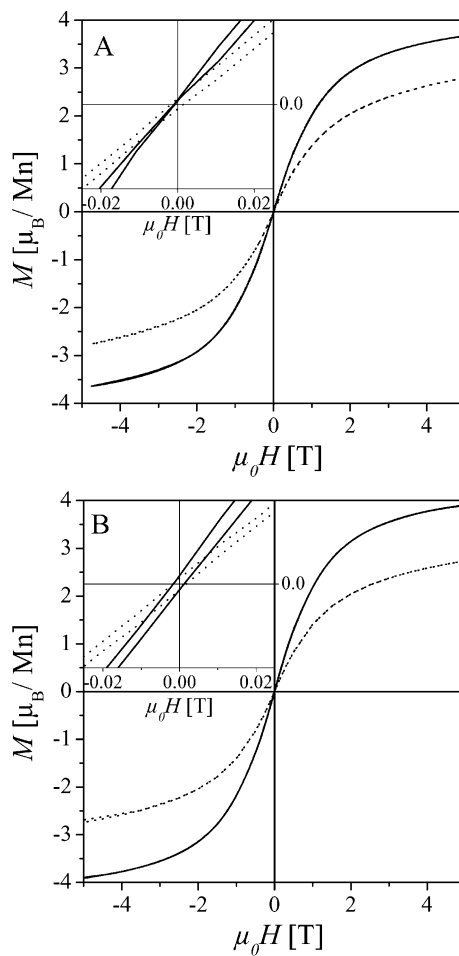


Figure 6. Hysteresis loops at $T = 2$ K for (A) samples from $\text{Mn}(\text{ac})_2$ with 1.39% Mn (solid line) and 4.38% Mn (dotted line) and (B) samples from $\text{Mn}(\text{acac})_3$ with 1.20% Mn (solid line) and 4.85% Mn (dotted line).

from antiferromagnetic coupling between the manganese atoms. At high field ($\mu_0 H = 5$ T), the magnetic moment per atom reaches 3.90 and 3.68 μ_B/Mn for the most diluted samples (Samples I and II) and 2.80 and 2.74 μ_B/Mn for the most concentrated ones (Samples III and IV). As a general trend, the magnetization does not reach saturation even at an applied field of 5 T. The magnetic moments at saturation determined from the fitting of the experimental curves with a Langevin function $M(H, T) = M_T L(\mu H/k_B T)$ are very close to the values determined from Curie constants obtained from susceptibility measurements.

The magnetization of diluted samples (I and II) provides a clear evidence for the presence of a majority of manganese in a low-oxidation state (Mn^{2+} , $3d^5$ or Mn^{3+} , $3d^4$; the expected effective moments are: Mn^{2+} 5.92 μ_B , Mn^{3+} 4.90 μ_B , and Mn^{4+} 3.87 μ_B). In the case of more concentrated samples (III and IV), the magnetization does not allow any conclusion, as the values are lower than that expected for any oxidation state. This result therefore supports the hypothesis of a coexistence of different manganese oxidation states in the zirconia matrix.

The low-field and high-field magnetic measurements provide clear evidence for a paramagnetic behavior with antiferromagnetic interactions that increase with the dopant concentrations from ca. 1 to ca. 5%. The manganese oxidation state is difficult to determine from the collected magnetic data. A purely Mn^{4+} or Mn^{3+} dopant state was already excluded on the basis of EPR measurements. Interestingly, the observed magnetic properties are not sensitive to the nature of the molecular source of manganese, that is, $\text{Mn}(\text{ac})_2$ or $\text{Mn}(\text{acac})_3$. This surprising result may be related to the synthetic route. It was already shown that the synthesis of Mn oxides by the “benzyl alcohol route” always leads to the formation of a secondary phase, which is MnO for the case of Mn_3O_4 and vice versa.^[36] In our case, the presence of Mn^{2+} in the samples synthesized from $\text{Mn}(\text{acac})_3$ can be explained by the soft reducing power of the benzyl alcohol. Furthermore, from quantitative EPR measurements and the derived magnetic moment, it follows that Mn^{2+} is not the only species obtained from the $\text{Mn}(\text{ac})_2$ precursor. As each Mn^{2+} diluted in zirconia requires the generation of one oxygen vacancy, manganese atoms with a higher oxidation state are more likely to substitute a zirconium atom for large concentrations.

Conclusions

In search for high-temperature, ferromagnetic, diluted magnetic semiconductors, zirconia doped with up to 5% of manganese was synthesized by the “benzyl alcohol route”. The synthetic approach led to the formation of homogeneously doped single-crystalline nanoparticles with diameters of 3–4 nm. As a positive side effect of the nanoscale, the cubic structure does not need to be stabilized by the addition of another cation. The environment of the manganese diluted into the zirconia matrix was probed by EPR. It was found that Mn^{II} and Mn^{III} coexist and that their

ratio depends only on the manganese concentration. Magnetic measurements show mainly paramagnetic behavior of the diluted spins in the matrix. For larger Mn concentrations, a small amount of antiferromagnetic interactions was found. The ferromagnetism predicted by the theoretical work of Ostanin^[1] et al. was not found even at low temperature. This can be explained by the low oxidation state of the manganese, which, in our case, was estimated to be between (II) and (III). In fact, a higher oxidation state is more likely to give rise to ferromagnetic interactions.^[1] Furthermore, the same theoretical study predicts that the Curie temperature increases with the concentration of manganese. To confirm or refute the theoretical results, careful control of the manganese oxidation state and the amount of oxygen vacancies, as well as an increase in the manganese concentration is required. This will be the focal points of future studies.

Experimental Section

Zirconium(IV) isopropoxide 2-propanol complex (99.9%), manganese(II) acetate (98%), manganese(III) acetylacetonate, and benzyl alcohol (99%) were purchased from Aldrich, stored in a glove box, and used as received.

All the syntheses were performed in a glove box. In a typical reaction, a Teflon cup with an inner volume of 45 mL was filled with zirconium(IV) isopropoxide 2-propanol complex (1.29 mmol), benzyl alcohol (20 mL), and an adequate quantity of dopant. The cup was inserted into a steel autoclave, sealed, removed from the glove box, and then heated at 230 °C for 2 d in a furnace. The resulting suspensions were centrifuged, and the resulting precipitates were meticulously washed with ethanol and acetone and then dried in air at 80 °C. The reaction produced nanocrystals of pure ZrO_2 as a white powder with a yield greater than 80% or slightly brown crystals when Mn^{II} and Mn^{III} dopants were added.

The X-ray powder diffraction (XRD) data were collected with an X'Pert MPD Philips diffractometer (Cu- K_α X-radiation at 40 kV and 50 mA). Transmission electron microscopy (TEM) was carried out with a Hitachi H-9000 microscope operating at 300 kV. High-resolution microscopy and EELS measurements were performed with a CM200FEG (Philips) microscope operating at 200 kV and equipped with a field-emission gun. Samples were prepared by depositing a drop of a suspension of particles in ethanol on a copper grid coated with an amorphous carbon film. Inductively coupled plasma-atomic emission spectrometry (ICP-AES) was realized in the Analytical Laboratories of University of Aveiro. The EPR experiments were performed at X band ca. 9.5 GHz with a Bruker ESP300 spectrometer with microwave powers between 0.02 and 200 mW. Temperature studies from 6 to 300 K were carried out by using an Oxford gas-flow cryostat. Magnetic properties were measured with a SuperQuantum Interference Design (SQUID) magnetometer MPMS XL7 in the temperature range 2–350 K and a field of 0–5 T. The temperature-dependent susceptibility was measured by using the DC procedure. The sample was cooled to 2 K under zero magnetic field, a low magnetic field (5 mT) was then applied and the data collected from 2 K to 350 K (zero-field cooled, ZFC). Field-cooled (FC) measurements were performed from 2 to 350 K with an applied field during the cooling.

Acknowledgments

This work was partially supported by the European Network of Excellence FAME and the Pessoa bilateral exchange programs. G. C. acknowledges the Fundação para a Ciência e a Tecnologia (FCT) for the PhD grant (SFRH/BD/28848/2006). C. Reibel is acknowledged for EPR and SQUID measurements. A. Pucci is acknowledged for experimental assistance.

- [1] S. Ostanin, A. Ernst, L. M. Sandratskii, P. Bruno, M. Dane, I. D. Hughes, J. B. Staunton, W. Hergert, I. Mertig, J. Kudrnovský, *Phys. Rev. Lett.* **2007**, *98*, 016101.
- [2] G. D. Yadav, J. J. Nair, *Microporous Mesoporous Mater.* **1999**, *33*, 1–48.
- [3] D. S. Lee, W. S. Kim, S. H. Choi, J. Kim, H. W. Lee, J. H. Lee, *Solid State Ionics* **2005**, *176*, 33–39.
- [4] S. P. S. Badwal, *Solid State Ionics* **2001**, *143*, 39–46.
- [5] J. K. Dewhurst, J. E. Lowther, *Phys. Rev. B* **1998**, *57*, 741–747.
- [6] P. Li, I. W. Chen, J. E. Penner-Hahn, *Phys. Rev. B* **1993**, *48*, 10063–10073.
- [7] M. S. Khan, M. S. Islam, D. R. Bates, *J. Mater. Chem.* **1998**, *8*, 2299–2307.
- [8] D. Gazzoli, G. Mattei, M. Valigi, *J. Raman Spectrosc.* **2007**, *38*, 824–831.
- [9] E. V. Stefanovich, A. L. Shluger, C. R. A. Catlow, *Phys. Rev. B* **1994**, *49*, 11560–11571.
- [10] K. Sasaki, J. Maier, *Solid State Ionics* **2000**, *134*, 303–321.
- [11] M. Yashima, K. Ohtake, M. Kakihana, H. Arashi, M. Yoshimura, *J. Phys. Chem. Solids* **1996**, *57*, 17–24.
- [12] G. Bacquet, J. Dugas, C. Escribe, F. Fabre, *J. Phys. C* **1973**, *6*, 1432–1443.
- [13] G. Bacquet, J. Dugas, C. Escribe, J. M. Gaité, J. Michoulier, *J. Phys. C* **1974**, *7*, 1551–1563.
- [14] P. J. Alonso, R. Alcalá, J. Casas-Gonzalez, R. Cases, V. M. Orera, *J. Phys. Chem. Solids* **1989**, *50*, 1185–1191.
- [15] M. Valigi, D. Gazzoli, R. Dragone, A. Marucci, G. Mattei, *J. Mater. Chem.* **1996**, *6*, 403–408.
- [16] M. Niederberger, G. Garnweitner, *Chem. Eur. J.* **2006**, *12*, 7282–7302.
- [17] M. Niederberger, G. Garnweitner, J. Buha, J. Polleux, J. Ba, N. Pinna, *J. Sol-Gel Sci. Technol.* **2006**, *40*, 259–266.
- [18] M. Niederberger, *Acc. Chem. Res.* **2007**, *40*, 793–800.
- [19] M. Niederberger, G. Garnweitner, N. Pinna, G. Neri, *Prog. Solid State Chem.* **2005**, *33*, 59–70.
- [20] G. Garnweitner, L. M. Goldenberg, O. V. Sakhno, M. Antonietti, M. Niederberger, J. Stumpe, *Small* **2007**, *3*, 1626–1632.
- [21] N. Pinna, G. Garnweitner, M. Antonietti, M. Niederberger, *Adv. Mater.* **2004**, *16*, 2196–2200.
- [22] G. Garnweitner, M. Niederberger, *J. Am. Ceram. Soc.* **2006**, *89*, 1801–1808.
- [23] R. C. Garvie, *J. Phys. Chem.* **1965**, *69*, 1238–1243.
- [24] R. C. Garvie, *J. Phys. Chem.* **1978**, *82*, 218–224.
- [25] J. C. Valmalette, M. Isa, *Chem. Mater.* **2002**, *14*, 5098–5102.
- [26] J. Joo, T. Yu, Y. W. Kim, H. M. Park, F. Wu, J. Z. Zhang, T. Hyeon, *J. Am. Chem. Soc.* **2003**, *125*, 6553–6557.
- [27] M. Gateshki, V. Petkov, T. Hyeon, J. Joo, M. Niederberger, Y. Ren, *Solid State Commun.* **2006**, *138*, 279–284.
- [28] F. Zhang, P. J. Chupas, S. L. A. Lui, J. C. Hanson, W. A. Caliebe, P. L. Lee, S. W. Chan, *Chem. Mater.* **2007**, *19*, 3118–3126.
- [29] G. H. Du, Z. Y. Yuan, G. V. Tendeloo, *Appl. Phys. Lett.* **2005**, *86*, 063113.
- [30] G. Bacquet, J. Dugas, C. Escribe, A. Rouanet, *J. Solid State Chem.* **1976**, *19*, 251–261.
- [31] C. C. Appel, N. Bonanos, A. Horsewell, S. Linderoth, *J. Mater. Sci. Lett.* **2001**, *36*, 4493–4501.
- [32] F. C. Jentoft, A. Hahn, J. Krohnert, G. Lorenz, R. E. Jentoft, T. Ressler, U. Wild, R. Schlogl, C. Haner, K. Kohler, *J. Catal.* **2004**, *224*, 124–137.
- [33] M. Occhiuzzi, D. Cordischi, R. Dragone, *Phys. Chem. Chem. Phys.* **2003**, *5*, 4938–4945.
- [34] J. Krzystek, J. Telser, L. A. Pardi, D. P. Goldberg, B. M. Hoffman, L. C. Brunel, *Inorg. Chem.* **1999**, *38*, 6121–6129.
- [35] G. Clavel, M. G. Willinger, D. Zitoun, N. Pinna, *Adv. Funct. Mater.* **2007**, *17*, 3159–3169.
- [36] I. Djerdj, D. Arcon, Z. Jaglicic, M. Niederberger, *J. Phys. Chem. C* **2007**, *111*, 3614–3623.

Received: September 14, 2007

Published Online: December 6, 2007